mater.scichina.com link.springer.com

Published online 19 June 2020 | https://doi.org/10.1007/s40843-020-1326-3
Sci China Mater 2021, 64(1): 61–72

Ultra-small interlayer spacing and nano channels in anionic layered perovskite $Cs_2Pb(SCN)_2I_2$ enable efficient photoelectric conversion

Yiming Li[1,3†], Jiangjian Shi[1†], Huijue Wu[1], Yanhong Luo[1,3,4], Dongmei Li[1,3,4] and Qingbo Meng[1,2,4*]

ABSTRACT **Due to distinctive lattice and electronic properties, the thiocyanate anion (SCN^-) perovskite as an alluring two-dimensional (2D) material system, can be applied in optoelectronic devices. Herein, both photovoltaic and photodetection performances of the 2D $Cs_2Pb(SCN)_2I_2$ have been investigated. Compared with the conventional cationic 2D perovskites, $Cs_2Pb(SCN)_2I_2$ possesses ultra-small interlayer spacing, additional interlayer nano channels, which is thus beneficial for charge transport ability. The planar heterojunction solar cell based on $Cs_2Pb(SCN)_2I_2$ as the light absorber, has presented the highest power conversion efficiency among long-chain-cation-based 2D perovskite devices. Besides, the $Cs_2Pb(SCN)_2I_2$-based photodetector also exhibits much higher photodetection performance (i.e. quantum efficiency, on/off ratio, responsivity, detectivity, response speed, polarization sensitivity and detection stability). It is thus suggested that these outstanding photoelectric characteristics of $Cs_2Pb(SCN)_2I_2$ could bring huge opportunities for its more abundant optoelectronic applications, such as field-effect transistor and light-emitting diodes.**

Keywords: 2D perovskite, thiocyanate anion, heterojunction solar cell, photodetector

INTRODUCTION

Two-dimensional (2D) materials have emerged as promising candidates for high-performance optoelectronic applications [1–4]. In addition to traditional materials like black phosphorus [5,6], graphene [7,8], and MoS_2 [9,10], layered organic-inorganic hybrid perovskites have attracted intensive interest due to their high optical absorption [11], high charge mobility [12], large specific surface area [13] and good stability [14]. Currently, 2D layered perovskites have been widely explored for photovoltaic, photodetection and light-emitting applications [15–17].

For typical 2D perovskites, metal and halogen atoms are connected through tight covalent bonds, resulting in inorganic layers comprised of octahedral cage frameworks, while long organic cations connect these inorganic layers through van der Waals interactions [18]. Compared with 3D perovskites, structural demanding on the anionic corner-sharing between the inorganic layers is fully released in the 2D perovskite, which could help to increase the lattice freedom and reduce the probability of defect formation [19]. As we know, fast charge transport channels usually exist along the in-plane direction of the inorganic layers. Charge transport across these layers can be realized mainly through the quantum tunneling effect, and the tunneling probability is correlated with interlayer spacing determined by the organic cations [20]. In the past few years, long-chain cations such as bulky butylammonium (BA), phenylethylammonium (PEA) and 1-naphthylmethylamine (NMA), have been mainly used as dielectric organic groups for 2D layered perovskite structures [21–30]. These long-chain cations and the resulting large interlayer spacing can effectively confine the carriers to realize high electron-photon conversion; however, it also limits the entire charge transport of the 2D perovskite optoelectronic devices. Manipulating ca-

[1] Key Laboratory for Renewable Energy, Chinese Academy of Sciences, Beijing Key Laboratory for New Energy Materials and Devices, Institute of Physics, Chinese Academy of Sciences, Beijing 100190, China
[2] Center of Materials Science and Optoelectronics Engineering, University of Chinese Academy of Sciences, Beijing 100049, China
[3] School of Physics Science, University of Chinese Academy of Sciences, Beijing 100049, China
[4] Songshan Lake Materials Laboratory, Dongguan 523808, China
† These authors contributed equally to this work.
* Corresponding author (email: qbmeng@iphy.ac.cn)

tion structures, such as the Dion-Jacobson (D-J) 2D perovskite [31–33], has been attempted to reduce the interlayer spacing thereof to make up for this deficiency.

Furthermore, 2D perovskite can also be constructed by using appropriate anion groups. Recently, thiocyanate anion (SCN^-) has been successfully introduced to form 2D perovskite light absorber ($(CH_3NH_3)_2Pb(SCN)_2I_2$) or as additives to promote the 3D perovskite crystallization [34–39]. Compared with those cation groups, SCN^- has much smaller chain length and moreover can contribute the electronic states of the perovskite material [40–42]. These properties are able to afford better interlayer and intralayer charge transport abilities, thus helping to improve the performance of layered perovskite optoelectronic devices.

Herein, we explored the photoelectric conversion applications (including photovoltaic and photodetection) of an anionic layered perovskite $Cs_2Pb(SCN)_2I_2$. Besides the ultra-small interlayer spacing benefiting from the small SCN^- anion, $Cs_2Pb(SCN)_2I_2$ perovskite also exhibits nanoscale phase segregation within the 2D framework, which may form nano channels to facilitate interlayer charge transport. Owing to these lattice and microstructure advantages, a photoelectric conversion efficiency (PCE) of 4.24% has been achieved for $Cs_2Pb(SCN)_2I_2$-based planar solar cell, which is the highest among long-chain-cation-based pure 2D perovskite devices. Moreover, the $Cs_2Pb(SCN)_2I_2$ has presented superior photodetection performance, polarization sensitivity and stability, compared with those of conventional cation layered perovskites and 3D perovskites. These outstanding photoelectric characteristics of the anionic 2D perovskite material system show more opportunities in applications for efficient optoelectronic devices.

EXPERIMENTAL SECTION

Materials

PbI_2 (99.9985%), *N*,*N*-dimethylformamide (DMF), dimethylsulfoxide (DMSO), chlorobenzene (CB), tert-butylpyridine (TBP, 99.999%), titanium isopropoxide (TTIP), *n*-butyl alcohol, and poly(methyl methacrylate) (PMMA) powder were purchased from Alfa Aesar. $Pb(SCN)_2$, $PbBr_2$ (99.999%), CsI, Al_2O_3 nanoparticles dispersed in isopropanol (20 wt.%), aluminum tri-*sec*-butoxide, and bis(trifluoromethane)sulfonimide lithium salt (Li-TFSI, 99.9985%) were obtained from Sigma-Aldrich. Methylammonium bromide (MABr) was from Shanghai Materwin New Materials Co., Ltd. Methylammonium iodide (MAI) and PEA iodide (PEAI) were obtained from Xi'an Polymer Light Technology Corp. Isopropyl alcohol was from Xilong Scientific. Spiro-OMeTAD was obtained from Luminescence Technology Corp. (Lumtec). Tris(2-(1*H*-pyrazol-1-yl)-4-tert-butylpyridine)-cobalt(III) tris(bis(trifluorom- ethylsulfonyl) imide) (FK209) was from Dyesol.

Film and device fabrication

For $MAPbX_3$ (X=I, Br), 0.8 mol L^{-1} PbX_2 and 0.8 mol L^{-1} MAX were dissolved in DMF and stirred overnight. The perovskite precursor solution was spin-coated at 5000 r min^{-1} for 40 s, and CB (120 μL) was poured onto the substrate within 5 s. Then the half-crystallization film was heated at 100°C in the glovebox for 20 min. For the $Cs_2Pb(SCN)_2I_2$, 0.8 mol L^{-1} $Pb(SCN)_2$ and 1.6 mol L^{-1} CsI were dissolved in the DMF/DMSO mixed solvent (*v*:*v*=5:5) and stirred overnight at 80°C. For the $(PEA)_2PbI_4$, 0.8 mol L^{-1} PbI_2 and 1.6 mol L^{-1} PEAI were dissolved in DMF/DMSO mixed solvent (*v*:*v*=5:5) and stirred overnight. All these 2D perovskite precursor solutions mentioned above were directly spin coated onto the Al_2O_3 substrates for film characterization, at 2000 r min^{-1} for 40 s, and CB was dropped onto the substrate at 30 s. For the Al_2O_3 substrates, the precursor solution was prepared by dissolving aluminum tri-*sec*-butoxide (80 μL) in isopropyl alcohol (2 mL) and then stirred overnight. This precursor solution was spin-coated onto the quartz glass at 5000 r min^{-1} for 40 s and then sintered at 500°C for 40 min [43]. These substrates were used for perovskite deposition in N_2 glovebox without any surface treatment. For PMMA, 5 mg mL^{-1} PMMA powder was dissolved in CB and stirred overnight. For perovskites, they were protected by a PMMA layer with about 150-nm thickness.

2D perovskite solar cells in our work were fabricated on transparent fluorine-doped tin oxide (FTO)-coated glass substrates. First, a mildly acidic solution of TTIP in *n*-butyl alcohol (0.125 mol L^{-1}) was spin-coated on the FTO glass at 3000 r min^{-1} for 20 s, and subsequently calcined at 500°C for 1 h to give a 30-nm-thick dense TiO_2 layer. The obtained TiO_2 substrates were treated with $TiCl_4$ aqueous solution (25 mmol L^{-1}) at 70°C for 10 min, and then dried with N_2 flow and finally sintered at 500°C for 1 h. [6,6]-phenyl-C61-butyric acid (PCBA, 0.1 mg mL^{-1}) in CB was spin-coated on the top of TiO_2 film [44]. Then, 2D perovskite precursor solutions mentioned above were directly spin-coated onto the substrates. Then, a 200-nm-thick spiro-OMeTAD layer was deposited by spin-coating on the top of the perovskite films at 3500 r min^{-1} for 30 s and then heated at 60°C for 10 min. The spiro-OMeTAD

solution was prepared by dissolving it in CB (60 mmol L^{-1}) with the additives of Li-TFSI, FK209 and TBP at doping molar ratios of 0.5, 0.03 and 3.3. Finally, 80-nm-thick Au electrodes were deposited *via* thermal evaporation at an atmospheric pressure of 10^{-7} Torr (Kurt J. Lesker).

After spin-coating the perovskite films on the Al_2O_3 substrates, 240 nm-thick Au electrodes were deposited through particular masks by vacuum thermal evaporation to obtain a lateral-structured photodetector device.

Characterizations

X-ray diffraction (XRD) spectra were measured with a Panalytical X-ray diffractometer with Cu Kα as the radiation source. The light absorption measurements were conducted using a UV-Visible spectrometer (Shimadzu 3600). The steady-state photoluminescence (PL) measurements were conducted using an Edinburgh fluorescence spectrometer (FLS 920). A 445 nm pulsed diode laser (EPL-445, ~4 mW cm^{-2}, 62 ps, 20 MHz) was used as the excitation source. A laser scanning confocal microscopy (WITec 300R) was used to probe the PL mapping of the perovskite film. A 532-nm laser was used to excite the perovskite film and the PL was measured by a charge-coupled device (CCD) array. Femtosecond transient absorption (TA) was detected using a pump-probe method to measure differential absorption spectra and their decay profiles. The output of a Coherent Astrella amplifier (35 fs pulses at 800 nm) was split into two parts. One part of the laser output pumped an optical parametric amplifier (OPerA-Solo) to generate pump pulses at 450 nm. The other part was used as probe after white light generation in a sapphire plate. The delay between the pump and the probe pulses was controlled by a motorized delay-stage and the signal was detected using a fiber optic spectrometer (Avantes, AvaSpec-ULS2048CL-EVO). The morphology of the samples was observed by using a scanning electron microscope (SEM) from Zeiss Sigma 300. For the current density-voltage (*J-V*) measurements, solar cell devices were illuminated under AM 1.5 simulated light (100 mW cm^{-2}) from Zolix SS150A. *J-V* curves were measured and recorded by a digital source meter (Keithley model 2602). The solar devices were taken out for external quantum efficiency (EQE) measurements using an Enli Tech (Taiwan, China) EQE measurement system. Photocurrent-voltage characteristics of the photodetectors were measured on a Keithley 2602 Source Meter under different illumination from a commercial blue light emitting diode (LED) at 465 nm. Modulated transient photocurrent (m-TPC) measurements were performed by a tunable nanosecond laser (Opotek, RADIANT 532 LD) pumped at 532 nm and recorded by a sub-nanosecond resolved digital oscilloscope (Tektronix, MDO3034) with input impedances of 50 Ω. A signal generator (Tektronix, AFG3052C) together with a low-pass filter was applied to give steady-state bias voltages over the cell.

RESULTS AND DISCUSSION

Fig. 1a depicts the representative structures of 2D layered perovskites, which can be constructed by either the long-chain amino cation or the pseudohalide anion. The cationic layered perovskite has been widely investigated previously [21–30], whereas the anionic layered perovskites have been rarely explored. For a layered perovskite, the charge transport across the inorganic layers is mainly realized by the quantum tunneling effect. The spaces between these layers are energy barriers because they have negligible contributions to electronic states near the conduction band minimum (CBM) or valence band maximum (VBM) [36]. Fig. 1b gives a simplified energy alignment to reflect this tunneling process. The lattice structure of a SCN^- anionic layered perovskite (for example, $(CH_3NH_3)_2Pb(SCN)_2I_2$ and $Cs_2Pb(SCN)_2I_2$) is schematically presented in Fig. 1c. For this type of materials, one Pb atom is surrounded by four halide atoms and two SCN^- groups. The halide atom is shared by two nearest-neighbored Pb atoms, thus forming a continuous Pb-I layer in the $a\times b$ plane. SCN^- terminates the periodic extension of the inorganic layer in the *c* direction. The exact structure of the $(CH_3NH_3)_2Pb(SCN)_2I_2$ was previously determined [41]. Here, we focus on the $Cs_2Pb(SCN)_2I_2$ because it can exhibit a much better film morphology than the $(CH_3NH_3)_2Pb(SCN)_2I_2$.

To make a direct comparison in the interlayer spacing, XRD patterns of four types of layered perovskite films with different cation/anion groups are presented in Fig. 1d [31,32]. All the perovskite films exhibit the crystal orientation along the [001] direction. The (002) and (004) diffraction peaks shifting to larger angles can be clearly observed, when the cation (or anion) size is decreased. With these diffraction angles, the interlayer spacings of $(NMA)_2PbBr_4$, $(PEA)_2PbI_4$, $(PDMA)PbI_4$ (PDMA=1,4-phenylenedimethanammonium), and $Cs_2Pb(SCN)_2I_2$ are calculated to be 19.0, 16.2, 12.4 and 9.1 Å, respectively. Fig. 1e gives quantitative comparison of the interlayer tunneling probabilities among these representative 2D perovskites by assuming the same energy barrier of 0.5 eV [45]. As the dashed arrows depicted in Fig. 1a, charge tunneling is considered to occur between the nearest-

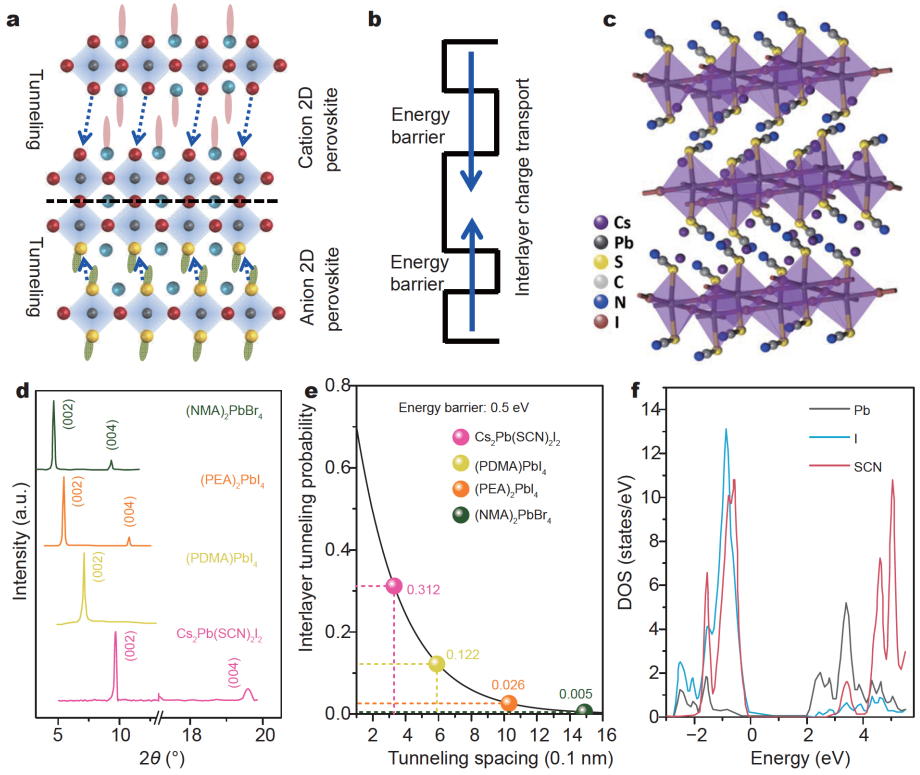

Figure 1 (a) Lattice structure of the layered perovskite constructed from long-chain cations or short-chain anions. The interlayer charge transfer is realized by the tunneling effect (depicted by dash arrows). (b) Schematic diagram of the electronic energy and interlayer charge transport process of the layered perovskites. (c) Schematic diagram of the crystal structure for the SCN^- anionic layered perovskite ($Cs_2Pb(SCN)_2I_2$). (d) XRD patterns of four types of layered perovskite films with different cation/anion groups. The $(NMA)_2PbBr_4$ and $(PDMA)PbI_4$ data are reorganized from Refs. [31,32]. (e) Computed correlation between the charge tunneling probability and interlayer spacing (energy barrier 0.5 eV) of these four types of layered perovskites. (f) Contribution of different atoms to the DOS of the SCN^--based perovskite. The data are reorganized from Ref. [41].

neighbored anions and the tunneling spacing is also derived after considering the Pb–S and Pb–I bond lengths. The tunneling probability of $Cs_2Pb(SCN)_2I_2$ reaches 0.312. This is more than ten times as high as that of the conventional Ruddlesden-Popper perovskite (NMA- and PEA-based systems) and is more than two times as high as that of the PDMA-based D-J layered perovskite. Notably, PDMA was reported to exhibit the smallest interlayer spacing amongst the cationic layered perovskites [31]. Moreover, SCN^- occupies a large proportion in the density of states (DOS) of the valence-band electronic states of the perovskite (Fig. 1f), which provides sufficient spaces for the charge tunneling [40–42]. These properties indicate that the SCN^- layered perovskite possesses better interlayer charge transport abilities, which could be the most promising 2D perovskite candidate for optoelectronic applications.

Firstly, we investigated the photophysical properties of the $Cs_2Pb(SCN)_2I_2$ film, including absorption, PL, and femtosecond TA, as presented in Fig. 2a–c. The perovskite exhibits an excitonic absorption peak at 575 nm and a cut-off edge at 585 nm. For the PL, only a weak peak appears near the band edge, whereas, a much stronger emission peak is observed in the long-wavelength region (at 670 nm). This long-wavelength emission arises from non-intrinsic electronic state of the film. For a much clearer overview of electronic states within the SCN-perovskite, TA measurement of the $Cs_2Pb(SCN)_2I_2$ film was carried out. Under a pulse excitation, three photobleaching (PB) and two photo-induced absorption (PA) bands are observed (Fig. 2b and c). The PB bands at 560 nm (PB1) and 579 nm (PB2) are located at similar positions, indicating that they result from the band-edge ground states. Compared with the PB, two stronger PA bands located at 540 and 590 nm are also observed, which exhibit similar dynamics behavior to that of the PB1/PB2. This implies that the PA bands come from the charge transfer from the band-edge states (e.g., VBM and CBM)

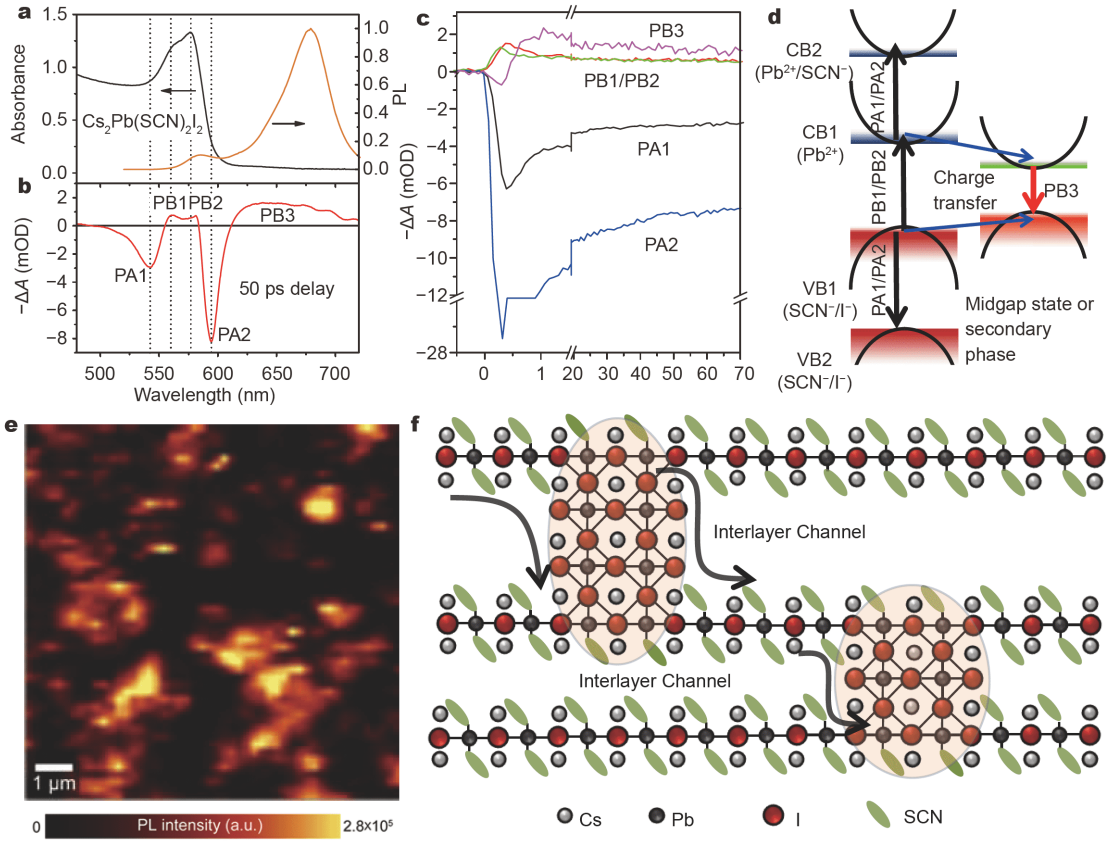

Figure 2 (a) Steady-state light absorption, PL emission and (b) femtosecond transient (50 ps after the photoexcitation) absorption spectra of the $Cs_2Pb(SCN)_2I_2$ film. (c) TA dynamics of different PA and PB bands, indicating a fast charge transfer towards PB3 band. (d) Schematic diagram of the charge transfer within the SCN^--based layered perovskite under light excitation. (e) Space-resolved confocal PL intensity mapping of the $Cs_2Pb(SCN)_2I_2$ film. (f) Schematic diagram of the interlayer charge transport process *via* the participation of nano phase-segregation interlayer channels for the $Cs_2Pb(SCN)_2I_2$-layered perovskite.

to higher-energy states. The PB3 (630–700 nm) is located at similar wavelength position to the PL emission. After the photoexcitation, the PB3 band rises to its peak at a relatively slow rate, within ~1 ps; while PB1, PB2, PA1 and PA2 bands experience a fast rise, then a partial decay within the early 600 fs. This difference between PB3 and other bands sends us a clear message of charge transfer, from band-edge states to mid-gap states of $Cs_2Pb(SCN)_2I_2$ or to low-bandgap secondary phases within the film. This charge transfer process is ultrafast, and it takes ~0.2 ps to complete the full charge transfer process. Based on the DOS of the 2D SCN^- perovskite (Fig. 1e) [41], the charge transfer processes within this perovskite are depicted in Fig. 2d. The mid-gap states can be deep defects [46], excitonic triplet [47–49] or recently widely investigated self-trapped excitons [50–52], whereas, the low-bandgap secondary phase may arise from the phase segregation in the perovskite film [53].

Space-resolved confocal laser scanning microscopy was used to map the PL of the $Cs_2Pb(SCN)_2I_2$ film. It is found that the luminescence intensity of the film (integrated from 600 to 750 nm) is extremely space-inhomogeneous; only several small-sized emission centers are observed (Fig. 2e). This is suggested to be due to the phase segregation in the film. Notably, the size of the emission centers has reached the spatial resolution limit of the instrument, indicating that the real emission center may be much smaller. The segregated phase is thus suggested to be 3D $CsPbI_3$ existing in nano scale because 3D perovskite is usually easy to form compared with 2D perovskite. Fig. 2f gives a possible structure of the phase segregation in the 2D framework. In the *c* direction, some Pb atoms may not be completely terminated by the SCN^- groups, which can covalently coordinate with I atoms to form localized PbI_6 octahedron structures, thus leading to the nano $CsPbI_3$ phase. These nano phases can directly

connect the neighbored inorganic layers. TA dynamics indicates that the charges generated in the 2D perovskite can transfer into these segregated phases within ~0.2 ps. This charge transfer is much faster than that observed in the NMA systems [54]. We believe that these nano phases can provide more effective charge transport channels than the pure tunneling effect. Therefore, the ultra-small interlayer spacing and nano channels in the $Cs_2Pb(SCN)_2I_2$ are supposed to be able to afford much better photoelectric conversion performance than the conventional cation layered perovskite. In the following, we will further study the photoelectric properties of $Cs_2Pb(SCN)_2I_2$ through its photovoltaic and photodetection devices.

Planar heterojunction solar cells were fabricated, of which the structure (FTO/c-TiO_2/PCBA/2D perovskite/Spiro-OMeTAD/Au) is depicted in Fig. 3a. Fig. 3b presents the top-view SEM image of the $Cs_2Pb(SCN)_2I_2$ film. Through optimizing the film deposition process, averaged grain size of over 3 μm was obtained, which is significantly larger than that of the conventional perovskite polycrystalline films [43,55,56]. These large grains would help to decrease grain boundaries and corresponding defects. Finally, PCE of 4.24% has been achieved from the $Cs_2Pb(SCN)_2I_2$-based device with a short-circuit current density (J_{SC}) of 12 mA cm^{-2}, open-circuit voltage (V_{OC}) of 1010 mV and fill factor (FF) of 0.35, as presented in Fig. 3c. Its low FF mainly arises from the relatively large series resistance of the cell. Normalized EQE of the $Cs_2Pb(SCN)_2I_2$ device is presented in Fig. 3d. The cell gives high and similar EQE response in the whole light absorption range (400–600 nm) and the photoelectric conversion from the excitonic absorption is also clearly seen. This indicates that photo-induced charges in the $Cs_2Pb(SCN)_2I_2$ film has been efficiently separated and collected, benefiting from the large heterojunction electric field and interlayer charge transport. Comparatively, conventional Ruddlesden-Popper 2D perovskite $(PEA)_2PbI_4$ presented negligible photovoltaic performance (PCE: 0.009%, inset of Fig. 3c). The J_{SC} of the device is only 0.06 mA cm^{-2}, two orders of magnitude lower than that of the $Cs_2Pb(SCN)_2I_2$ device. This giant difference confirms the advantage of $Cs_2Pb(SCN)_2I_2$ in the charge transport.

For clarity, a direct comparison of the cell efficiency of $Cs_2Pb(SCN)_2I_2$ to those of $(PEA)_2PbI_4$ and other previously reported pure long-chain-cation 2D perovskites (A_2PbI_4 or $BPbI_4$, A: long-chain monoamine ions, B: long-chain diamine ions) is summarized and presented in Fig. 3e and Table 1 [31,33,57–61]. It can be clearly seen

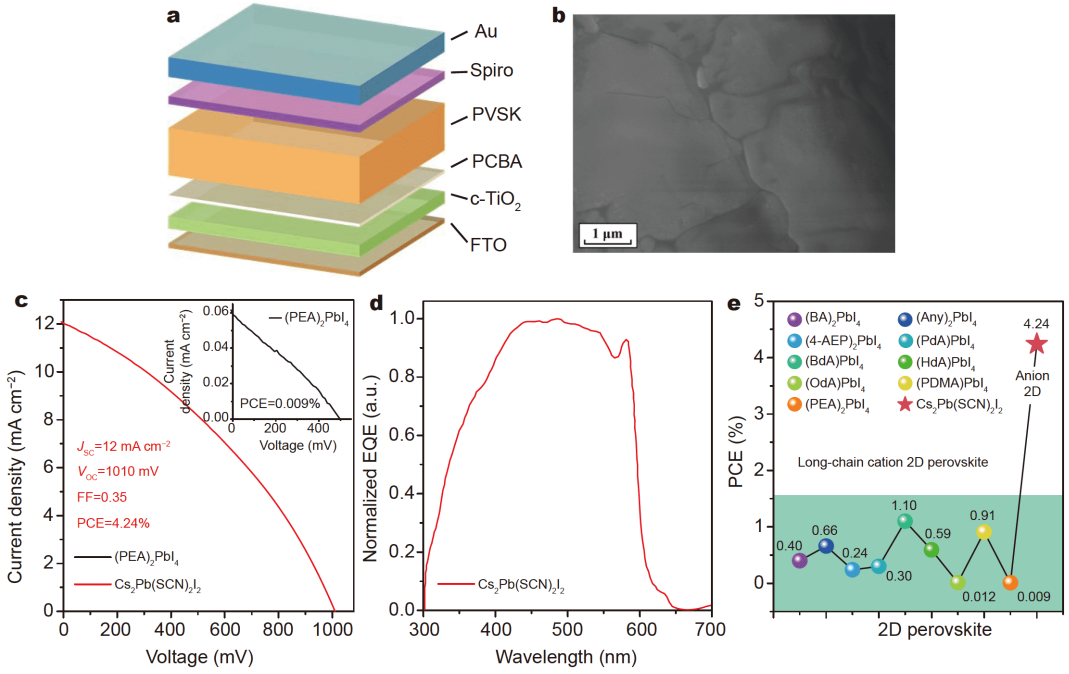

Figure 3 (a) Schematic diagram of the device structure for 2D perovskite-based planar solar cells; (b) SEM image of the $Cs_2Pb(SCN)_2I_2$ film deposited on Al_2O_3 substrate; (c) photoelectric conversion performance of the $Cs_2Pb(SCN)_2I_2$- and $(PEA)_2PbI_4$-based planar solar cells; (d) normalized EQE characterization of the $Cs_2Pb(SCN)_2I_2$ device; (e) comparison of the cell efficiency obtained here with that of previously reported pure long-chain-cation 2D perovskites devices [31,33,57–61].

that almost all the 2D cationic perovskites can only exhibit low efficiencies of <1%. To our knowledge, except for MA_2PbI_4 perovskite [57], our $Cs_2Pb(SCN)_2I_2$-based cell exhibits the highest efficiency among all the pure 2D perovskite devices. This result also implies a potential application of the SCN^- perovskite, which could be an excellent interface-layered structure for highly efficient 3D perovskite solar cells.

Due to the superior film crystallization, high photocharge separation and collection, and reduced probability of defect formation, efficient photodetector can also be expected based on the $Cs_2Pb(SCN)_2I_2$. Here, we fabricated a kind of lateral-structured photodetector device (photoconductor) on a quartz/Al_2O_3 substrate with electrode spacing of 80 μm, as schematically shown in Fig. 4a and Fig. S1. Compared with the photodiode, the photoconductor is much easier to produce and no electrical window layer is needed. This makes the photoconductor have more flexibility in material choice and extending the photodetection wavelength. For comparison, 2D $(PEA)_2PbI_4$, 3D $MAPbI_3$ and $MAPbBr_3$ are also used as the photodetector active layers. Fig. 4b presents the current density-voltage characteristics of the $Cs_2Pb(SCN)_2I_2$-based photodetector under 465 nm LED illumination. Illuminated at this wavelength, the SCN^- perovskite exhibits the second lowest light absorption among these four materials (Fig. S2). Under +15 V bias voltage, the device gives relatively low dark current density of ~2×10^{-4} mA cm^{-2} (~0.6 nA), whereas, under +5 V, the dark current is only 0.2 nA. This result is much lower than that of other three perovskite devices (Fig. S3), but comparable to that of commercialized Si photodiodes (Photodiodes [Online]. Thorlabs. https://www.thorlabs-china.cn/newgrouppage9.cfm?objectgroup_id=285). Low dark current can not only increase the photodetection limit of weak light but also lower the power dissipation. It is worth noting that bias voltage is not an issue for perovskite photoconductors here, because commercial photodetectors are often required to ensure device performance (IR Photoconductive Detectors [Online]. Thorlabs. https://www.thorlabs.com/newgrouppage9.cfm?objectgroup_id=6479; Mounted Photodiodes [Online]. Thorlabs. https://www.thorlabs.com/newgrouppage9.cfm?objectgroup_id=1285).

Under 9.0 mW cm^{-2} light illumination and +15 V bias voltage, the current response increases to ~3 mA cm^{-2}, exhibiting an EQE of >80% [62]. Under weaker light illumination (for example, ~3 μW cm^{-2}), the EQE can approach 1000%, which may benefit from the avalanche effect [63]. For the 3D perovskite, the avalanche effect is much weaker, implying that the carrier confinement in the 2D perovskite plays a vital role in enhancing the carrier-carrier or carrier-lattice interactions. For the $(PEA)_2PbI_4$ perovskite, its EQE is only 5% under a 7.5 mW cm^{-2} illumination, and its weak-light EQE is also much lower than that of $Cs_2Pb(SCN)_2I_2$. These results demonstrate that the $Cs_2Pb(SCN)_2I_2$ in a lateral-structured device also exhibits much higher photoelectric conversion than other perovskites studied here. Fig. 4c gives the photocurrent response (I_{ph}) of the $Cs_2Pb(SCN)_2I_2$ device to the light intensity (I_{exc}), which presents a power-law relationship as $I_{ph}=I_{exc}^{0.7}$. This relationship implies that the charge recombination increases at higher light intensities because of the relatively large electrode spacing. The on/off ratios of these perovskite photodetectors under about 9 mW cm^{-2} with different bias voltages are derived, as shown in Fig. 4d. The $Cs_2Pb(SCN)_2I_2$ device presents a large on/off ratio of over 10^4 at the bias of +15 V, which is about two orders of magnitude larger than that of other three devices. This

Table 1 Representative pure 2D Pb-based perovskite absorbers constructed by long-chain cations and their photovoltaic performances

2D perovskite	Device structure	PCE (%)	Year [Ref.]
BA_2PbI_4	FTO/c-TiO_2/BA_2PbI_4/Spiro-OMeTAD/Au	0.40	2018 [57]
$(Any)_2PbI_4$	FTO/c-TiO_2/m-TiO_2/$(Any)_2PbI_4$/Spiro-OMeTAD/Au	0.66	2017 [58]
$(4\text{-}AEP)_2PbI_4$	FTO/C_{60}/$(4\text{-}AEP)_2PbI_4$/Spiro-OMeTAD/Au	0.24	2019 [59]
$(PdA)PbI_4$	FTO/c-TiO_2/$(PdA)PbI_4$/Spiro-OMeTAD/Au	0.30	2019 [33]
$(BdA)PbI_4$	FTO/c-TiO_2/m-TiO_2/$(BdA)PbI_4$/Spiro-OMeTAD/Au	1.10	2017 [60]
$(HdA)PbI_4$	FTO/c-TiO_2/m-TiO_2/$(HdA)PbI_4$/Spiro-OMeTAD/Ag	0.59	2016 [61]
$(OdA)PbI_4$	FTO/c-TiO_2/m-TiO_2/$(OdA)PbI_4$/Spiro-OMeTAD/Ag	0.012	2016 [61]
$(PDMA)PbI_4$	FTO/c-TiO_2/m-TiO_2/$(PDMA)PbI_4$/Spiro-OMeTAD/Au	0.91	2019 [31]
$(PEA)_2PbI_4$	FTO/c-TiO_2/PCBA/$(PEA)_2PbI_4$/Spiro-OMeTAD/Au	0.009	This work
$Cs_2Pb(SCN)_2I_2$	FTO/c-TiO_2/PCBA/$Cs_2Pb(SCN)_2I_2$/Spiro-OMeTAD/Au	4.24	This work

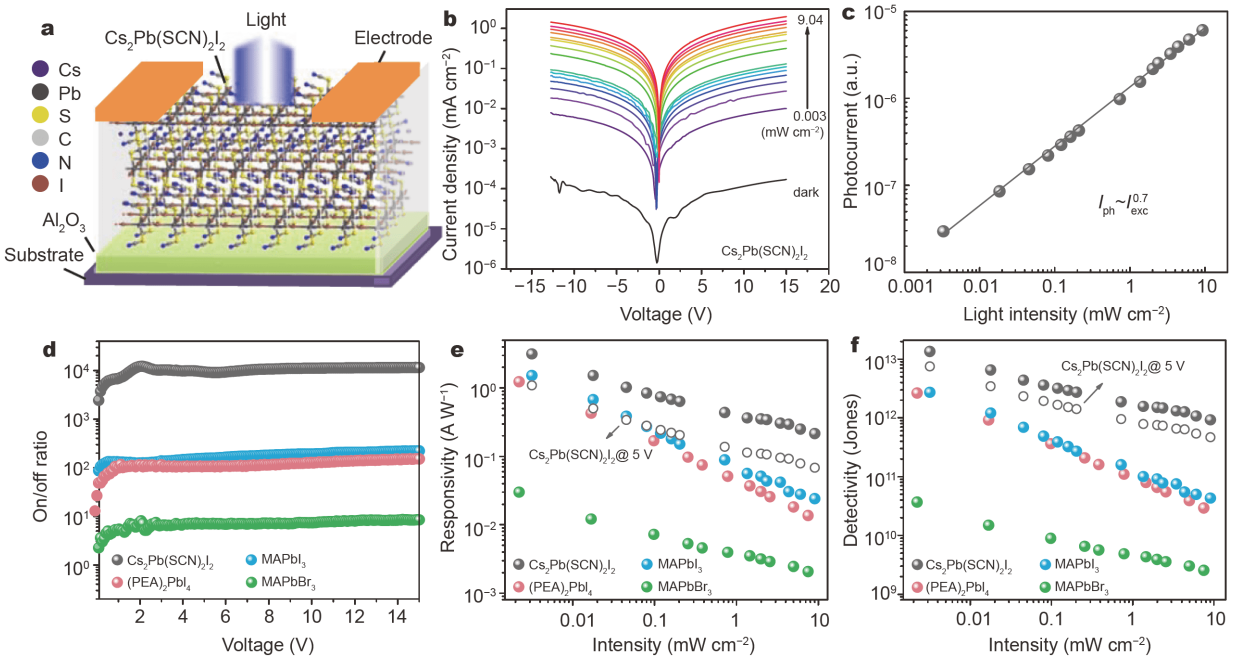

Figure 4 (a) Device structure of the lateral-structured polycrystalline $Cs_2Pb(SCN)_2I_2$ perovskite photodetector; (b) *J-V* curve of the $Cs_2Pb(SCN)_2I_2$ device measured under the dark as well as 465 nm LED irradiation with various illumination intensities; (c) dependence of the photocurrent (I_{ph}) to the light intensity (I_{exc}) for $Cs_2Pb(SCN)_2I_2$ device across the entire illumination region; (d) on/off ratio of the lateral photodetector based on four different perovskite materials with different bias voltages under 9 mW cm^{-2} illumination intensity; (e) photoresponsivities and (f) detectivities of these four devices under a fixed +15 V bias and illumination intensities ranging from 0.003 to 10 mW cm^{-2}. The photodetection performance of the $Cs_2Pb(SCN)_2I_2$ device under a +5 V bias is also presented by open circle plots.

advantage arises from lower dark current and better photocurrent response. In our opinion, the higher photocurrent response mainly benefits from the better charge transport ability and lower charge recombination. The ultra-small interlayer spacing, nano channels and large polycrystalline grains enable the high charge transport, while the 2D structure and the strong covalent coordination between Pb and SCN^- may help suppress the defect formation.

Photodetection responsivities (R) and detectivities (D^*) of these devices are further derived by quantifying their current-light intensity responses [64,65]. Some representative photodetection parameters are summarized in Table 2. Fig. 4e shows the R values for these devices fixed under +15 V bias and illumination intensities ranging from 0.003 to 10 mW cm^{-2}. Similar to most of the perovskite photodetectors, the R exhibits a decreasing trend with increasing light intensity [66]. At illumination intensity of 3 μW cm^{-2}, the R of the $Cs_2Pb(SCN)_2I_2$ device reaches 3 A W^{-1}, much higher than that of the $(PEA)_2PbI_4$ and $MAPbI_3$ devices (~1.2 A W^{-1}). Under high illumination intensity of 10 mW cm^{-2}, the $Cs_2Pb(SCN)_2I_2$ can still maintain an R of 0.2 A W^{-1}, which is almost one order of magnitude higher than those of $(PEA)_2PbI_4$ and $MAPbI_3$ devices. The detectivity ($D^*=R/(2qJ_{dark})^{1/2}$, where q is the electron charge and J_{dark} is the dark current density) for these devices, are presented in Fig. 4f [64,65]. At the illumination intensity of 3 μW cm^{-2}, the D^* of the $Cs_2Pb(SCN)_2I_2$ device reaches 1.5×10^{13} Jones, which is about five times as high as those of the $(PEA)_2PbI_4$ and $MAPbI_3$ devices. This D^* is even higher than those of the conventional Ge photodiode, PbS and PbSe photoconductor devices [67–69]. Under higher illumination intensity of 10 mW cm^{-2}, the D^* of the $Cs_2Pb(SCN)_2I_2$ device is still maintained at a level of 10^{12} Jones. These properties demonstrate that the SCN^- perovskite can maintain relatively high detection activity over much wider light intensity ranges. Under a lower bias voltage of +5 V, the $Cs_2Pb(SCN)_2I_2$ device can still exhibit excellent photodetection performance, as shown by the open circle plots in Fig. 4e and f. Specially, across the entire illumination region, the D^* is much higher than those of all the other perovskite devices operated under a +15 V bias.

We further find that the $Cs_2Pb(SCN)_2I_2$ device exhibits polarization sensitivity. The schematic diagram of the polarization measurement is shown in Fig. 5a and the polarization angle-dependent photocurrent responses for these studied devices are presented in Fig. 5b. Apparently,

Table 2 Photodetection performances of the perovskite devices

Perovskite	Dark current (nA)		EQE (%)		On/off ratio at 9 mW cm^{-2}	R (A W^{-1})		D^* (10^{10} Jones)	
	5 V	15 V	3 μW cm^{-2}	100 μW cm^{-2}		3 μW cm^{-2}	100 μW cm^{-2}	3 μW cm^{-2}	100 μW cm^{-2}
$Cs_2Pb(SCN)_2I_2$	0.2	0.6	10^3	290	1.1×10^4	3	0.86	1500	360
$(PEA)_2PbI_4$	0.75	1.8	330	60	1.8×10^2	1.0	0.18	280	42
$MAPbI_3$	1.5	3.0	400	80	2.1×10^2	1.2	0.24	290	44
$MAPbBr_3$	1.8	6.0	10	3	10	0.03	0.008	4	0.85

$Cs_2Pb(SCN)_2I_2$ is the only one that can exhibit polarization sensitivity. This is an interesting result because the polarization response is mostly realized through oriented low-dimensional single crystal [70-73] which has rarely been found within polycrystalline materials. According to the lattice structure, it is suggested that the orientation of the non-spherical electron cloud distribution of the SCN^- group is the most possible origin [40–42]. The photon-electron interaction of the perovskite is supposed to be closely related to the relative orientation between the polarized light and the SCN^- group, thus resulting in an in-plane anisotropy of polarization photodetection response, as schematically shown by an amplified scheme in Fig. 5a. Although the PEA may also have molecular orientation, no polarization response was observed because the PEA almost has no contribution to the band-edge electronic states of the $(PEA)_2PbI_4$ [74]. Thus, these findings provide a simpler route to construct polarization-sensitive photodetector, that is, using polycrystalline SCN^- anonic layered perovskite films.

The response speed of these perovskite photodetectors were further determined by studying the on/off rise and fall times (time difference between the 0.1 and 0.9 times of peak photocurrent) [64]. As in Fig. 5c, the $Cs_2Pb(SCN)_2I_2$ device exhibits rise and fall times of 32 and 36 μs, respectively, which are much shorter than that of the $MAPbI_3$ device. Faster response of the $Cs_2Pb(SCN)_2I_2$ was also observed than that of $(PEA)_2PbI_4$ and $MAPbBr_3$, as reflected by the TPC measurements (Fig. S4) [75]. This fast response finally results in a high photodetection bandwidth of 10^5 Hz, one order of magnitude higher than those of $MAPbI_3$ devices, as presented

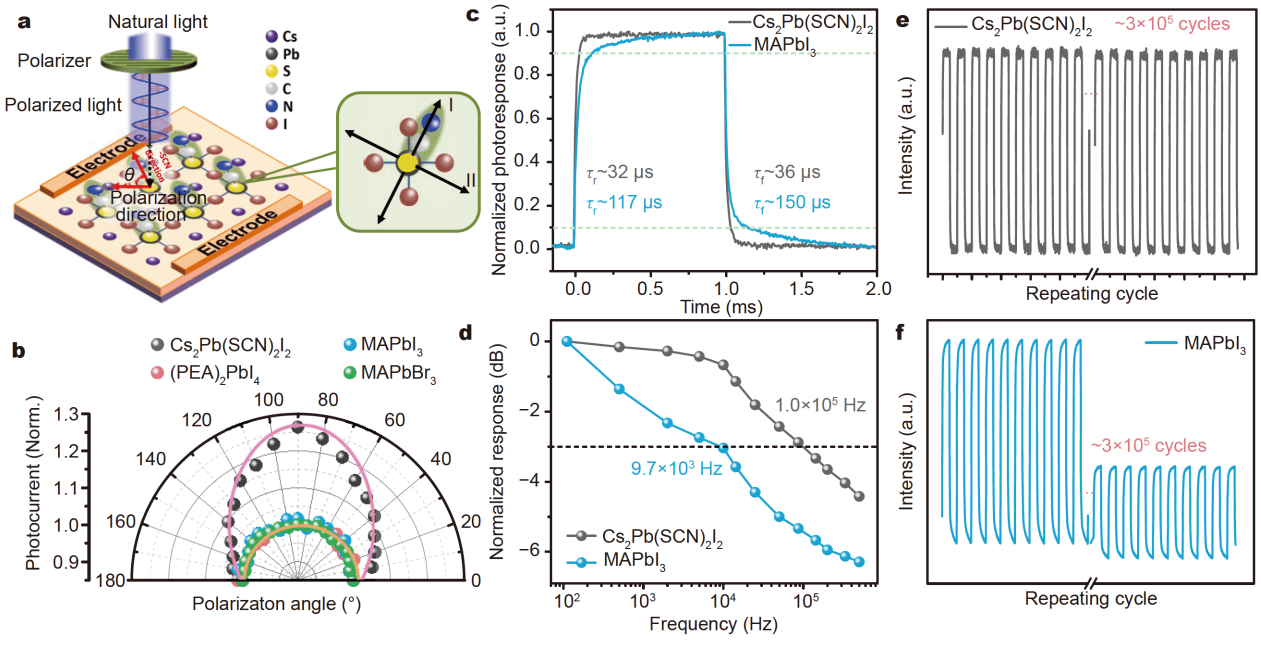

Figure 5 (a) Schematic diagram of the polarization sensitivity measurement and relative orientation between the polarized light (adjusted by a polarizer) and the SCN^- group; (b) polarization sensitivity of these polycrystalline perovskite photodetectors; (c) rise and fall time of the $Cs_2Pb(SCN)_2I_2$ and $(PEA)_2PbI_4$ devices. The time is determined according to the time difference between the 0.1 and 0.9 times of peak photocurrent (dashed lines). (d) Photodetection bandwidth of the $Cs_2Pb(SCN)_2I_2$ and $MAPbI_3$ devices; (e) continuous measurements of the $Cs_2Pb(SCN)_2I_2$ photodetector over 3×10^5 on/off cycles; (f) continuous measurements of the $MAPbI_3$ photodetector over 3×10^5 on/off cycles.

in Fig. 5d [76]. By designing the device structure (such as reducing the electrode spacing), we believe the response speed can be further promoted, which opens up a potential application of the $Cs_2Pb(SCN)_2I_2$ in the optical communication.

The detection stability of the $Cs_2Pb(SCN)_2I_2$ device was evaluated by measuring the continuous on/off performances [77]. As shown in Fig. 5e, almost no degradation of the dark or photocurrent is observed over 3×10^5 cycles. The response speed is neither influenced by the on/off cycling (Fig. S5). In contrast, for the $MAPbI_3$ device, only half of the photocurrent response is maintained after the continuous on/off cycles (Fig. 5f) and the response velocity is also slowed down (Fig. S5). The degradation of the 3D perovskite device is mainly due to the ion migration under electric field of 10^5 V m^{-1}. Notably, this field strength is much weaker than that in a perovskite diode. Thus, even for a perovskite photodiode, its detection stability needs more concerned. In contrast, for a $Cs_2Pb(SCN)_2I_2$ device, the covalent coordination between Pb and SCN^- helps to suppress the ion migration along the edge of Pb-I inorganic frameworks, thereby improving the device photoelectric stability.

CONCLUSION

The photoelectric characteristics of an anionic layered perovskite $Cs_2Pb(SCN)_2I_2$ have been studied in this work. Compared with conventional cationic layered perovskite, $Cs_2Pb(SCN)_2I_2$ possesses ultra-small interlayer spacing and interlayer nano channels, thus yielding better charge transport ability. By using this perovskite as the light absorber layer in a planar heterojunction solar cell, power conversion efficiency of 4.24% has been achieved, which is the highest among all the long-chain-cation-based pure 2D perovskite devices. Besides, the superior charge transport and photoelectric conversion of $Cs_2Pb(SCN)_2I_2$ can further realize high-performance perovskite photodetectors. The $Cs_2Pb(SCN)_2I_2$-based photoconductor has exhibited much higher photodetection EQE, on/off ratio, responsivity, detectivity, response speed, interesting polarization sensitivity and more importantly detection stability. All these outstanding photoelectric characteristics benefit from the lattice and film microstructure of the $Cs_2Pb(SCN)_2I_2$, which may have opportunities in abundant optoelectronic application, such as field-effect transistor and light-emitting diodes.

Received 11 March 2020; accepted 1 April 2020; published online 19 June 2020

1 Zhang T, Xie L, Chen L, *et al. In situ* fabrication of highly luminescent bifunctional amino acid crosslinked 2D/3D $NH_3C_4H_9COO(CH_3NH_3PbBr_3)_n$ perovskite films. Adv Funct Mater, 2017, 27: 1603568
2 Novoselov KS, Geim AK, Morozov SV, *et al.* Electric field effect in atomically thin carbon films. Science, 2004, 306: 666–669
3 Lee C, Wei X, Kysar JW, *et al.* Measurement of the elastic properties and intrinsic strength of monolayer graphene. Science, 2008, 321: 385–388
4 Novoselov KS, Geim AK, Morozov SV, *et al.* Two-dimensional gas of massless Dirac fermions in graphene. Nature, 2005, 438: 197–200
5 Eswaraiah V, Zeng Q, Long Y, *et al.* Black phosphorus nanosheets: Synthesis, characterization and applications. Small, 2016, 12: 3480–3502
6 Zhang D, Yuan Z, Zhang G, *et al.* Preparation and characterization of black phosphorus. Acta Chim Sin, 2018, 76: 537–542
7 Sun D, Aivazian G, Jones AM, *et al.* Ultrafast hot-carrier-dominated photocurrent in graphene. Nat Nanotech, 2012, 7: 114–118
8 Zhao Y, Xie L, Ma L, *et al.* Preparation and application of polydimethylsiloxane encapsulated graphene-based flexible infrared detector. Acta Chim Sin, 2020, 78: 161–169
9 Jariwala D, Sangwan VK, Wu CC, *et al.* Gate-tunable carbon nanotube-MoS_2 heterojunction p-n diode. Proc Natl Acad Sci USA, 2013, 110: 18076–18080
10 Liu Z. MoS_2-OH bilayer-mediated growth of inch-sized monolayer MoS_2 on arbitrary substrates. Acta Phys-Chim Sin, 2019, 35: 1309–1310
11 Grinblat G, Abdelwahab I, Nielsen MP, *et al.* Ultrafast all-optical modulation in 2D hybrid perovskites. ACS Nano, 2019, 13: 9504–9510
12 Kagan C, Mitzi D, Dimitrakopoulos C. Organic-inorganic hybrid materials as semiconducting channels in thin-film field-effect transistors. Science, 1999, 286: 945–947
13 Dou L, Wong AB, Yu Y, *et al.* Atomically thin two-dimensional organic-inorganic hybrid perovskites. Science, 2015, 349: 1518–1521
14 Zhang X, Wu G, Yang S, *et al.* Vertically oriented 2D layered perovskite solar cells with enhanced efficiency and good stability. Small, 2017, 13: 1700611
15 Wu G, Li X, Zhou J, *et al.* Fine multi-phase alignments in 2D perovskite solar cells with efficiency over 17% *via* slow post-annealing. Adv Mater, 2019, 31: 1903889
16 Qi X, Zhang Y, Ou Q, *et al.* Photonics and optoelectronics of 2D metal-halide perovskites. Small, 2018, 14: 1800682
17 Cortecchia D, Yin J, Petrozza A, *et al.* White light emission in low-dimensional perovskites. J Mater Chem C, 2019, 7: 4956–4969
18 Cohen BE, Li Y, Meng Q, *et al.* Dion-Jacobson two-dimensional perovskite solar cells based on benzene dimethanammonium cation. Nano Lett, 2019, 19: 2588–2597
19 Kim J, Ho-Baillie A, Huang S. Review of novel passivation techniques for efficient and stable perovskite solar cells. Sol RRL, 2019, 3: 1800302
20 Milot RL, Sutton RJ, Eperon GE, *et al.* Charge-carrier dynamics in 2D hybrid metal-halide perovskites. Nano Lett, 2016, 16: 7001–7007
21 Gao L, Zhang F, Chen X, *et al.* Enhanced charge transport by incorporating formamidinium and cesium cations into two-dimensional perovskite solar cells. Angew Chem, 2019, 131: 11863–11867
22 Jiang Y, He X, Liu T, *et al.* Intralayer A-site compositional en-

gineering of Ruddlesden-Popper perovskites for thermostable and efficient solar cells. ACS Energy Lett, 2019, 4: 1216–1224
23 Fu W, Liu H, Shi X, *et al.* Tailoring the functionality of organic spacer cations for efficient and stable quasi-2D perovskite solar cells. Adv Funct Mater, 2019, 29: 1900221
24 Zhang F, Kim DH, Lu H, *et al.* Enhanced charge transport in 2D perovskites *via* fluorination of organic cation. J Am Chem Soc, 2019, 141: 5972–5979
25 Yuan M, Quan LN, Comin R, *et al.* Perovskite energy funnels for efficient light-emitting diodes. Nat Nanotech, 2016, 11: 872–877
26 Byun J, Cho H, Wolf C, *et al.* Efficient visible quasi-2D perovskite light-emitting diodes. Adv Mater, 2016, 28: 7515–7520
27 Wang N, Cheng L, Ge R, *et al.* Perovskite light-emitting diodes based on solution-processed self-organized multiple quantum wells. Nat Photon, 2016, 10: 699–704
28 Zou W, Li R, Zhang S, *et al.* Minimising efficiency roll-off in high-brightness perovskite light-emitting diodes. Nat Commun, 2018, 9: 608
29 Zhang F, Lu H, Tong J, *et al.* Advances in two-dimensional organic-inorganic hybrid perovskites. Energy Environ Sci, 2020
30 Yang X, Zhang X, Deng J, *et al.* Efficient green light-emitting diodes based on quasi-two-dimensional composition and phase engineered perovskite with surface passivation. Nat Commun, 2018, 9: 570
31 Li Y, Milić JV, Ummadisingu A, *et al.* Bifunctional organic spacers for formamidinium-based hybrid Dion-Jacobson two-dimensional perovskite solar cells. Nano Lett, 2019, 19: 150–157
32 Yu M, Yi C, Wang N, *et al.* Control of barrier width in perovskite multiple quantum wells for high performance green light-emitting diodes. Adv Opt Mater, 2019, 7: 1801575
33 Ahmad S, Fu P, Yu S, *et al.* Dion-Jacobson phase 2D layered perovskites for solar cells with ultrahigh stability. Joule, 2019, 3: 794–806
34 Tai Q, You P, Sang H, *et al.* Efficient and stable perovskite solar cells prepared in ambient air irrespective of the humidity. Nat Commun, 2016, 7: 11105
35 Jiang Q, Rebollar D, Gong J, *et al.* Pseudohalide-induced moisture tolerance in perovskite $CH_3NH_3Pb(SCN)_2I$ thin films. Angew Chem Int Ed, 2015, 54: 7617–7620
36 Ke W, Xiao C, Wang C, *et al.* Employing lead thiocyanate additive to reduce the hysteresis and boost the fill factor of planar perovskite solar cells. Adv Mater, 2016, 28: 5214–5221
37 Liu J, Shi J, Li D, *et al.* Molecular design and photovoltaic performance of a novel thiocyanate-based layered organometal perovskite material. Synth Met, 2016, 215: 56–63
38 Daub M, Hillebrecht H. Synthesis, single-crystal structure and characterization of $(CH_3NH_3)_2Pb(SCN)_2I_2$. Angew Chem Int Ed, 2015, 54: 11016–11017
39 Lou Y, Niu Y, Yang D, *et al.* Rod-shaped thiocyanate-induced abnormal band gap broadening in SCN^- doped $CsPbBr_3$ perovskite nanocrystals. Nano Res, 2018, 11: 2715–2723
40 Xiao Z, Meng W, Saparov B, *et al.* Photovoltaic properties of two-dimensional $(CH_3NH_3)_2Pb(SCN)_2I_2$ perovskite: A combined experimental and density functional theory study. J Phys Chem Lett, 2016, 7: 1213–1218
41 Tang G, Yang C, Stroppa A, *et al.* Revealing the role of thiocyanate anion in layered hybrid halide perovskite $(CH_3NH_3)_2Pb(SCN)_2I_2$. J Chem Phys, 2017, 146: 224702
42 Labram JG, Venkatesan NR, Takacs CJ, *et al.* Charge transport in a two-dimensional hybrid metal halide thiocyanate compound. J Mater Chem C, 2017, 5: 5930–5938
43 Li Y, Li Y, Shi J, *et al.* High quality perovskite crystals for efficient film photodetectors induced by hydrolytic insulating oxide substrates. Adv Funct Mater, 2018, 28: 1705220
44 Dong Y, Li W, Zhang X, *et al.* Highly efficient planar perovskite solar cells *via* interfacial modification with fullerene derivatives. Small, 2016, 12: 1098–1104
45 Sakurai JJ, Napolitano J. Modern Quantum Mechanics. San Francisco: Addison-Wesley, 2014
46 Leroux M, Grandjean N, Beaumont B, *et al.* Temperature quenching of photoluminescence intensities in undoped and doped GaN. J Appl Phys, 1999, 86: 3721–3728
47 Kropp JL, Dawson WR, Windsor MW. Radiative and radiationless processes in aromatic molecules. Pyrene. J Phys Chem, 1969, 73: 1747–1752
48 Sajoto T, Djurovich PI, Tamayo AB, *et al.* Temperature dependence of blue phosphorescent cyclometalated Ir(III) complexes. J Am Chem Soc, 2009, 131: 9813–9822
49 Younts R, Duan HS, Gautam B, *et al.* Efficient generation of long-lived triplet excitons in 2D hybrid perovskite. Adv Mater, 2017, 29: 1604278
50 Zhang L, Wu L, Wang K, *et al.* Pressure-induced broadband emission of 2D organic-inorganic hybrid perovskite $(C_6H_5C_2H_4NH_3)_2PbBr_4$. Adv Sci, 2019, 6: 1801628
51 Yu J, Kong J, Hao W, *et al.* Broadband extrinsic self-trapped exciton emission in Sn-doped 2D lead-halide perovskites. Adv Mater, 2018, 31: 1806385
52 Zhou L, Liao J, Huang Z, *et al.* Intrinsic selftrapped emission in 0D lead-free $(C_4H_{14}N_2)_2In_2Br_{10}$ single crystal. Angew Chem, 2019, 131: 15581–15586
53 Halder A, Chulliyil R, Subbiah AS, *et al.* Pseudohalide (SCN^-)-doped $MAPbI_3$ perovskites: A few surprises. J Phys Chem Lett, 2015, 6: 3483–3489
54 Xing G, Wu B, Wu X, *et al.* Transcending the slow bimolecular recombination in lead-halide perovskites for electroluminescence. Nat Commun, 2017, 8: 14558
55 Yang Y, Wu J, Wang X, *et al.* Suppressing vacancy defects and grain boundaries *via* Ostwald ripening for high-performance and stable perovskite solar cells. Adv Mater, 2019, 32: 1904347
56 Lin C, Lee J, Kim J, *et al.* Origin of open-circuit voltage enhancements in planar perovskite solar cells induced by addition of bulky organic cations. Adv Funct Mater, 2019, 30: 1906763
57 Zhu X, Xu Z, Zuo S, *et al.* Vapor-fumigation for record efficiency two-dimensional perovskite solar cells with superior stability. Energy Environ Sci, 2018, 11: 3349–3357
58 Rodríguez-Romero J, Hames BC, Mora-Seró I, *et al.* Conjugated organic cations to improve the optoelectronic properties of 2D/3D perovskites. ACS Energy Lett, 2017, 2: 1969–1970
59 Li Y, Cheng H, Zhao K, *et al.* 4-(Aminoethyl)pyridine as a bifunctional spacer cation for efficient and stable 2D Ruddlesden-Popper perovskite solar cells. ACS Appl Mater Interfaces, 2019, 11: 37804–37811
60 Safdari M, Phuyal D, Philippe B, *et al.* Impact of synthetic routes on the structural and physical properties of butyl-1,4-diammonium lead iodide semiconductors. J Mater Chem A, 2017, 5: 11730–11738
61 Safdari M, Svensson PH, Hoang MT, *et al.* Layered 2D alkyldiammonium lead iodide perovskites: Synthesis, characterization, and use in solar cells. J Mater Chem A, 2016, 4: 15638–15646
62 Liu Y, Sun J, Yang Z, *et al.* 20-mm-large single-crystalline for-

mamidinium-perovskite wafer for mass production of integrated photodetectors. Adv Opt Mater, 2016, 4: 1829–1837
63 Sze SM, Ng KK. Physics of Semiconductor Devices. Hoboken: John Wiley & Sons, 2006
64 Wang H, Kim DH. Perovskite-based photodetectors: materials and devices. Chem Soc Rev, 2017, 46: 5204–5236
65 Liu Y, Zhang Y, Yang Z, *et al.* Thinness- and shape-controlled growth for ultrathin single-crystalline perovskite wafers for mass production of superior photoelectronic devices. Adv Mater, 2016, 28: 9204–9209
66 Lian Z, Yan Q, Lv Q, *et al.* High-performance planar-type photodetector on (100) facet of $MAPbI_3$ single crystal. Sci Rep, 2015, 5: 16563
67 Saran R, Curry RJ. Lead sulphide nanocrystal photodetector technologies. Nat Photon, 2016, 10: 81–92
68 Rogalski A. History of infrared detectors. Opto-Electron Rev, 2012, 20: 279–308
69 Rauch T, Böberl M, Tedde SF, *et al.* Near-infrared imaging with quantum-dot-sensitized organic photodiodes. Nat Photon, 2009, 3: 332–336
70 Li SX, Zhang GP, Xia H, *et al.* Template-confined growth of Ruddlesden-Popper perovskite micro-wire arrays for stable polarized photodetectors. Nanoscale, 2019, 11: 18272–18281
71 Zhan Y, Wang Y, Cheng Q, *et al.* A butterfly-inspired hierarchical light-trapping structure towards a high-performance polarization-sensitive perovskite photodetector. Angew Chem, 2019, 131: 16608–16614
72 Ghoshal D, Wang T, Tsai H-, *et al.* Catalyst-free and morphology-controlled growth of 2D perovskite nanowires for polarized light detection. Adv Opt Mater, 2019, 7: 1900039
73 Zhou Y, Luo J, Zhao Y, *et al.* Flexible linearly polarized photodetectors based on all-inorganic perovskite $CsPbI_3$ nanowires. Adv Opt Mater, 2018, 6: 1800679
74 Zhao YQ, Ma QR, Liu B, *et al.* Layer-dependent transport and optoelectronic property in two-dimensional perovskite: $(PEA)_2PbI_4$. Nanoscale, 2018, 10: 8677–8688
75 Bao C, Chen Z, Fang Y, *et al.* Low-noise and large-linear-dynamic-range photodetectors based on hybrid-perovskite thin-single-crystals. Adv Mater, 2017, 29: 1703209
76 Dou L, Yang YM, You J, *et al.* Solution-processed hybrid perovskite photodetectors with high detectivity. Nat Commun, 2014, 5: 5404
77 Li L, Liu X, Li Y, *et al.* Two-dimensional hybrid perovskite-type ferroelectric for highly polarization-sensitive shortwave photodetection. J Am Chem Soc, 2019, 141: 2623–2629

Acknowledgements This work was supported by the National Key R&D Program of China (2018YFB1500101), the National Natural Science Foundation of China (11874402, 51421002, 51627803, 91733301 and 51761145042), and the International Partnership Program of Chinese Academy of Sciences (112111KYSB20170089).

Author contributions Li Y, Shi J and Meng Q conceived the idea. Li Y performed the device fabrication and measurements. Shi J designed the experiment and did the photophysical measurements. Li Y and Shi J did the data analysis. Li D, Luo Y and Wu H supported the measurement system construction, device fabrication, characterization and discussion. Li Y, Shi J and Meng Q participated in manuscript writing and revising. Shi J and Li D polished the language. All the authors were involved in the discussion and approved the manuscript. Li Y and Shi J contributed equally to this work.

Conflict of interest The authors declare no competing interest.

Supplementary Information Supporting data are available in the online version of the paper.

Yiming Li received the BS degree from Nankai University in 2015. She is now a PhD candidate in condensed matter physics at the Institute of Physics, Chinese Academy of Sciences (CAS) under the supervision of Prof. Qingbo Meng. Her research interests focus on charge carrier dynamics and charge loss mechanism in new-generation solar cells.

Jiangjian Shi obtained his PhD degree from the Institute of Physics, CAS in 2017. Now, he is an associate professor at the Institute of Physics, CAS. His research interest includes investigation on charge carrier dynamics, interfacial charge transfer and surface modification in new-generation solar cells.

Qingbo Meng is now a professor at the Institute of Physics, CAS. He received his PhD degree in 1997 from Changchun Institute of Applied Chemistry, CAS. His current research interest focuses on solar energy materials and technologies as well as the research of the dynamics of electron injection, diffusion and recombination in solar cells.

基于超小层间距和纳米通道的阴离子层状钙钛矿$Cs_2Pb(SCN)_2I_2$的高效光电转换

李一明[1,3†], 石将建[1†], 吴会觉[1], 罗艳红[1,3,4], 李冬梅[1,3,4], 孟庆波[1,2,4*]

摘要 硫氰酸根阴离子(SCN)钙钛矿材料由于拥有独特的晶格和电子性能使其成为光电应用中诱人的二维(2D)材料系统. 由此, 我们研究了2D结构$Cs_2Pb(SCN)_2I_2$材料的光伏和光电探测性能. 与常规的阳离子2D钙钛矿材料相比, $Cs_2Pb(SCN)_2I_2$具有极小的层间间距和额外的层间纳米通道, 从而大大提高了电荷传输能力. 对比所有基于长链阳离子的单纯2D钙钛矿器件, 以$Cs_2Pb(SCN)_2I_2$作为光吸收层的平面异质结太阳能电池表现出最高的光电转换效率. 此外, 基于$Cs_2Pb(SCN)_2I_2$的光电探测器表现出更高的光电探测EQE、开/关比、响应度、探测率、响应速度、偏振灵敏度以及更优异的光电稳定性. 所有这些出色的光电特性为SCN钙钛矿材料在更丰富的光电应用领域(例如: 场效应晶体管和发光二极管等)提供了巨大机遇.

